

Coherent control of total transmission of light through disordered media

S. M. Popoff, A. Goetschy, S. F. Liew, A. D. Stone, and H. Cao*
Department of Applied Physics, Yale University, New Haven, CT 06511, USA
(Dated: March 4, 2019)

We demonstrate order of magnitude coherent control of the total transmission through a disordered slab by shaping the wavefront of the input light. To understand the effect of finite illumination area on the maximum values of total transmission, we develop a model based on random matrix theory that reveals the role of long-range correlations. Predictions are confirmed by numerical simulations and shed light on our experimental results.

PACS numbers: 42.25.Bs, 05.60.Cd, 02.10.Yn

A lossless strong scattering medium, that has a thickness L much larger than the elastic mean free path ℓ , is normally opaque to incident beams of light, with only a small fraction, ℓ/L , of the incident photon flux diffusively transmitted. However, it has been known for over two decades that, due to the coherence of elastic scattering, this transmitted flux is not totally random in character, but has subtle correlations that were first discovered in the context of mesoscopic electron transport [1–4]. One striking implication of these correlations is that an optimally prepared coherent input beam could be transmitted through a strong scattering medium hundreds of mean free paths in thickness with order unity efficiency. These highly transmitting input states are eigenvectors of the matrix $t^\dagger t$, where t is the transmission matrix (TM) of the sample. They were predicted using a Random Matrix Theory (RMT) approach [1–3] and were termed “open channels”.

Because the input electron states are not controllable in mesoscopic conductors, the open channel concept was not testable there, except indirectly through other properties such as conductance fluctuations or shot noise. In strong scattering optical media the advent of wavefront shaping methods using a Spatial Light Modulator (SLM) have reopened the search for this dramatic effect. More generally, it has been shown that wavefront shaping of input states combined with feedback optimization can allow diverse functions for multiple scattering media in optics [5], causing them to act as lenses, phase plates [6, 7] or spectral filters [8, 9]. However coherent control of *total* transmission, which relies on mesoscopic correlations, is much more difficult. Some progress in this direction has been made by coupling incident light to highly transmissive channels, by focusing light on tight spots [10] or by measuring the partial TM and injecting light into calculated singular vectors [11]; here we report a further significant step: order of magnitude variation of total transmission via an SLM-based system through a strong scattering medium with average transmission $\sim 5\%$. We show that these results imply the presence of significant mesoscopic correlations in the diffusive transmission.

A major reason for the difficulty of demonstrating these effects is that previous theory assumed a bounded waveguide geometry, with full coherent control of all input channels, whereas experiments at optical frequencies are usually done in an unbounded three-dimensional slab geometry with in-

complete channel control (ICC). Recent theoretical work has shown that even in the waveguide geometry with N propagating modes, when the fraction of controlled channels, m , is much less than $\bar{T} = \ell/L$ — the average transmission probability with complete channel control — the mesoscopic correlations of long range are unobservable and the statistical properties revert to those of uncorrelated random matrices, described by the Marcenko-Pastur (MP) distribution [12], for which large coherent enhancement in transmission is not possible [13]. Previous experiments that measure only a small part of the transmission matrix are consistent with this conclusion [14, 15].

The open channel concept has also been shown to apply to the slab geometry [3], but only for an input beam with numerical aperture unity which also covers the entire sample surface. Below, we study the coherent control of transmission for a focused input spot, the typical experimental geometry. In this situation, one may achieve an input aperture close to unity, but the input channels are spatially localized in a finite illumination area, and the maximum possible enhancement of transmission is unknown. We present a quantitative theoretical solution to this remaining problem in coherent diffusion below, showing that its transmission eigenvalue density belongs to the family of distributions derived in Ref. [13], with a channel control parameter, m , which depends on the long-range mesoscopic correlations, and can be calculated microscopically.

Following the theoretical work described above, we expect to progressively lose the long-range mesoscopic correlations as the control of incident channels is reduced or when a small fraction of the output modes is measured [13]. To ensure a high degree of control of incoming waves, we designed a setup to control the phase of the optical field for both polarizations on an illumination area much larger than the wavelength. The experimental apparatus is presented in Fig.1(a) and detailed in [16]. To control independently the two polarizations, a polarizing beam splitter attached to a right-angle prism separates the two polarizations of the laser beam that are modulated by different areas of a phase-only SLM. The cube and the prism are mounted in the same holder to eliminate independent reflective elements in the two paths, thus dramatically reducing phase fluctuations in the interferometric setup [16]. The modulated wavefront is projected onto the pupil of a microscope

objective of numerical aperture 0.95. Adjacent pixels of the SLM are grouped to form “macro-pixels”, whose size determines the illumination area on the sample. In order to collect light in all output channels, we place the sample directly onto a large photodetector. This allows us to measure the total transmitted light without being limited by the numerical aperture of the collecting optics. Two additional photodetectors are used to measure the incident light intensity right before the microscope objective and the reflection from the sample. We then perform a feedback optimization procedure similar to the sequential algorithm developed in [17] to increase or decrease the total transmission. The value to optimize is the ratio of the transmitted intensity over the input intensity, henceforth termed the transmission, T . This point is crucial, since wave-front shaping by the SLM modifies not only the transport of light through the sample, but also the transmission of the optical systems that delivers light from the SLM to the sample, and is hence vulnerable to systematic errors or artifacts [18].

The scattering samples used in our experiment are slabs of randomly-packed TiO_2 microparticles, deposited on the glass cover slips by evaporation. The mean free path, measured from the coherent backscattering experiment, is $\ell = 0.8 \pm 0.1 \mu\text{m}$. To demonstrate coherent control we both maximize and minimize T . In Figure 1(b) and 1(c) we show results for a sample of average transmission $\langle T \rangle \sim 5\%$ that demonstrate an enhancement of $T \sim 3.6$, and a reduction ~ 3.1 . Thus the total transmission of a single realization of a scattering medium can be tuned by more than a factor of 11 between 1.6% and 18%. The diameter of the illumination area on the sample surface is $8.3 \mu\text{m}$, and the number of macro-pixels of the SLM, whose phases are optimized, is $N_{\text{in}} = 1740$. We also measure the change in reflection R (the ratio of the reflected light intensity over the incident intensity), and compare to the change expected from the transmission using the relation $R/\langle R \rangle = (1 - T)/(1 - \langle T \rangle)$ [Fig. 2(b) right]. The good agreement confirmed that the variations of the transmitted intensity measured are due to changes of the total transmission through the scattering sample. The main source of possible artifacts is unintentional compensation of optical aberrations or misalignment of the optical system. Such corrections would correspond to regular patterns of the SLM with low spatial frequencies, which are absent in the optimal phase masks shown in [16].

The important role of the mesoscopic correlations in the control of total transmission can be illustrated by comparing our data to the predictions of the uncorrelated random matrix ensemble. For an uncorrelated TM described by the MP law, the mean maximum transmission eigenvalue satisfies [12]:

$$\frac{\langle T^{\text{max}} \rangle}{\langle T \rangle} = (1 + \sqrt{\gamma})^2, \quad (1)$$

where γ is the ratio of the number of controlled input channels to the number of excited output channels. A reasonable estimate for its value is $\gamma \simeq (D/D_{\text{out}})^2$, where D_{out} is the typical size of the output diffusive halo. Hence the maximum possible transmission relative to the mean is monotonically decreasing

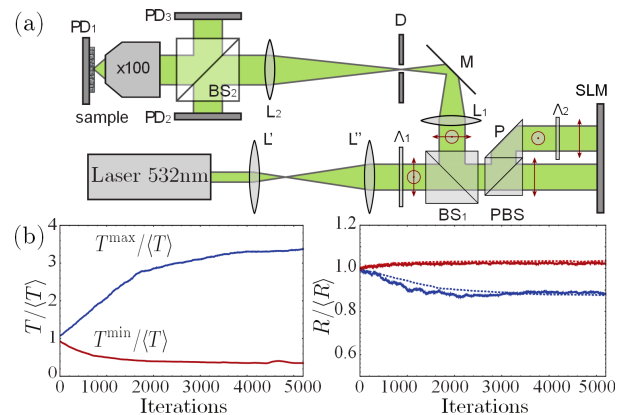


FIG. 1: (color online) (a) A schematic of the experimental setup for the control of total transmission. The output from a Nd:YAG laser, $\lambda = 532 \text{ nm}$, is expanded by two lenses (L' , L''). The two polarizations of light are separated by a polarizing beam splitter (PBS) and a prism (P) into two beams, and projected onto a phase-only SLM. The reflected beams are recombined into one beam, of which each polarization can be independently modulated in phase. The surface of the SLM is imaged onto the entrance pupil of the microscope objective. The scattering sample is placed at the focal plane of the objective. Three photodetectors, PD_1 , PD_2 and PD_3 , measure respectively the intensities of transmitted, incident and reflected light. (b) Measured $T/\langle T \rangle$ (left panel) and $R/\langle R \rangle$ (right panel) vs. the optimization step for enhancement (blue curve) and reduction (red curve) of the total transmission. The sample is $20 \mu\text{m}$ thick, and the average transmission $\langle T \rangle \sim 5\%$. The dotted line represents the reflection estimated from the transmission using $R/\langle R \rangle = (1 - T)/(1 - \langle T \rangle)$.

with the thickness of the sample, L , because D_{out} decreases with L for a fixed input illumination diameter, D . In Fig. 2(a) we plot $T^{\text{max}}/\langle T \rangle$ measured versus L for a fixed D , finding that instead of decreasing, it increases and then saturates at the largest L shown. The value of the enhancement at the largest L is more than twice that of the MP law. Similarly, for fixed L and variable D , the MP law predicts almost no transmission enhancement possible for small D and a slow linear increase for $D < L$; the data in Fig. 2(b) shows that even for $D \ll L$ the transmission enhancement is roughly a factor of two, and it increases more rapidly than the MP law predicts. In both cases, the experimental enhancements are much higher than the predictions of the uncorrelated model, implying that there exists significant correlations in the TM, which permit larger coherent control of emission.

To further confirm this, we now intentionally spoil the correlations by increasing the illumination diameter, which increases the total number of input channels, but without increasing the number of *controlled* input channels, denoted by N_{in} . This should reduce the transmission enhancement towards the MP value. We first use an illumination diameter of $3.6 \mu\text{m}$ and run the optimization algorithm controlling all 460 independent macro-pixels on the SLM. We gradually increase the illumination diameter to $12.4 \mu\text{m}$ by decreasing the size of the macro-pixels. The total number N_{tot} of macro-pixels, each corresponding to an independent input channel, increases. We

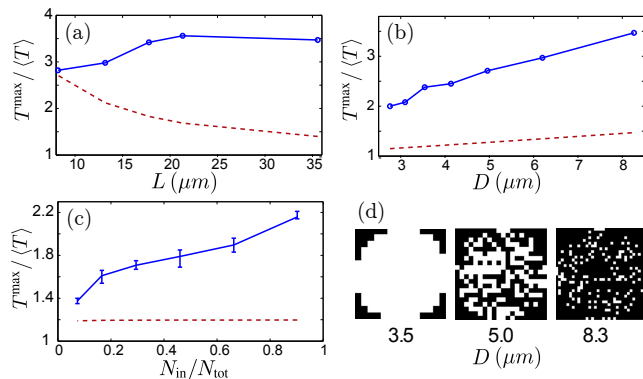


FIG. 2: (color online) (a) Maximal enhancement of total transmission $T^{\max}/\langle T \rangle$ as a function of the sample thickness L for an illumination diameter of $D = 8.3 \mu\text{m}$. (b) $T^{\max}/\langle T \rangle$ as a function of the input illumination diameter D for a fixed sample thickness $L = 30 \mu\text{m}$. Experimental data are shown by blue dots (connected by blue solid lines), and the estimation by Eq. (1) in red dotted lines. (c) Maximal enhancements of the total transmission as a function of the fraction of controlled input channels $N_{\text{in}}/N_{\text{tot}}$. The experimental data are blue dots with the error bars from ensemble measurements, the dotted red curve represents the prediction of Eq. (1) for uncorrelated systems. (d) Representative amplitude patterns of the SLM macro-pixels for three illumination diameters D . The dark macro-pixels are switched off, the white ones are on and their phases are optimized.

run the optimization process using only $N_{\text{in}} = 460$ randomly selected independent macro-pixels. We present in Fig. 2(c) schematics of the SLM patterns for three illumination diameter D . The uncontrolled macro-pixels are switched off by printing a high spatial frequency pattern on the SLM. Light incident on these macro-pixels is diffracted and filtered out by the iris at the Fourier plane. The maximal enhancement of total transmission $\langle T^{\max} \rangle / \langle T \rangle$ is plotted in Fig. 2(d) versus the fraction of controlled input channels $N_{\text{in}}/N_{\text{tot}}$. It is evident that the incomplete channel control progressively suppresses the effect of mesoscopic correlations, and the enhancement of total transmission decreases continuously. For a large illumination area, only a small fraction of the macro-pixels are chosen, and they are nearly independent. Consequently, $\langle T^{\max} \rangle / \langle T \rangle$ becomes comparable to the value from the uncorrelated model.

To get a quantitative understanding of previous results, we develop a theoretical model that takes into account the effect of a focused spot illumination on the transmission through a disordered slab. For this purpose, we make use of the filtered random matrix (FRM) ensemble, recently introduced to describe the role of incomplete channel control (ICC) in experimental measurements [13]. Assuming a bounded waveguide geometry, and the known eigenvalue density of $t^{\dagger}t$, the authors calculated the eigenvalue density of the matrix $\tilde{t}^{\dagger}\tilde{t}$, where \tilde{t} is the randomly filtered transmission matrix, with only a fraction m_1 (m_2) of the input (output) channels controlled (measured). A universal family of FRM densities parameterized by m_1, m_2, \bar{T} was obtained. An important assumption of the model is that all channels in the TM, whether measured

or not, play an equivalent “role” with respect to the scattering process. This is always true for channels represented by waveguide modes (or plane waves) because the latter all diffuse equivalently inside the sample. This property of ICC in momentum space has been confirmed by the agreement of the theory with numerical simulations of the filtered TM of a slab illuminated with a finite numerical aperture [13].

In general, this assumption does not hold for spatial filtering, as in the case of illumination with a focused spot, where the diffusion halo spreads out within the sample and points at the edge of the input are not equivalent to those in the middle. We find that for a waveguide of length L and width W with $L \gg W$ this effect is minimal, but in the current experimental configuration of a wide slab, where light never diffuses to the sample boundaries in the transverse direction, the correlated input changes the physics substantially. Nevertheless, extensive simulations reveal that this configuration is still described by the universal family of FRM densities obtained in [13], with an effective value of the input parameter, m_1 , and with $m_2 \approx 1$, (since all the transmitted light is collected). The effective parameter, m_1 , found numerically, is not simply related to the illumination diameter, but instead is determined by the following relation [13]:

$$m_1 = \frac{\text{Var } \tilde{T}}{\text{Var } T}, \quad (2)$$

where T and \tilde{T} are the eigenvalues of $t^{\dagger}t$ and $\tilde{t}^{\dagger}\tilde{t}$, respectively. We refer to this quantity as the normalized variance. This relationship for m_1 is exact within the original bounded waveguide model for the FRM; we now make the ansatz that it holds in this open slab geometry. In [16] we confirm the validity of this ansatz from the numerical solution of the wave equation in both two and three dimensions; the numerical method is the same as used to generate the data shown in Figs. 3 and 4 (described below).

Having established numerically that the normalized variance determines the desired eigenvalue density, we are able to formulate an analytic theory for this quantity using the diagrammatic methods developed for coherent wave transport [4, 19]. Using $\text{Var } T = 2\bar{T}/3 - \bar{T}^2$ where $\bar{T} = \ell/L$ [22], and decomposing $\langle \tilde{T}^2 \rangle$ as the product of four Green’s functions of the wave equation, we show in [16] that m_1 can be accurately expressed as

$$m_1 = \frac{1}{2/3 - \bar{T}} \left[\int d\mathbf{q} \frac{I(\mathbf{q})I(-\mathbf{q})}{(2\pi)^{d-1}I(\mathbf{q}=0)} F(\mathbf{q}) - \bar{T} \right], \quad (3)$$

where d is the space dimension, $I(\mathbf{q})$ is the Fourier transform of the transverse input intensity profile and $F(\mathbf{q})$ is the kernel that gives rise to the long-range correlation of the speckle pattern, which is described by the C_2 correlation function [19]. More specifically, the correlation between the total transmissions of two input channels with transverse momenta \mathbf{q}_a and $\mathbf{q}_a + \mathbf{q}$ is $C_2(\mathbf{q}) = F(\mathbf{q})/g$, where g is the dimensionless conductance. Its long range character is due to interference of pairs of diffusive paths that interact through a Hikami vertex

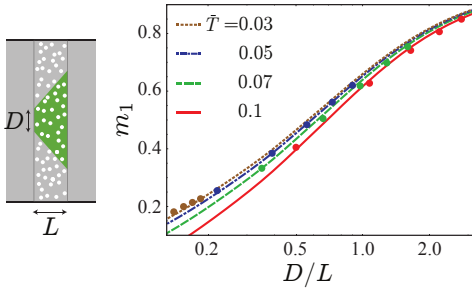


FIG. 3: (color online) Normalized variance (2) of the transmission eigenvalue density of a two-dimensional disordered slab, for different values of the illumination diameter D and the slab thickness L . Numerical results (dots) are obtained from the simulation of the wave equation with dielectric function $\epsilon(\mathbf{r}) = n_0^2 + \delta\epsilon(\mathbf{r})$; $n_0 = 1.3$ and $\delta\epsilon(\mathbf{r})$ uniformly distributed between $[-1.02, 1.02]$ in the slab and $\delta\epsilon(\mathbf{r}) = 0$ in free space. The four sets of points correspond to the thickness $kL = 120, 187, 280, 450$. The solid lines represent the theoretical prediction (3), where $I(\mathbf{q}) = D \text{sinc}(qD/2)$ and $\bar{T} = \langle T \rangle$ is found from the simulations with uniform illumination.

with a probability $1/g$. The effect of the finite illumination area is taken into account by the factor $I(\mathbf{q})I(-\mathbf{q})/I(\mathbf{q} = \mathbf{0})$ in Eq. (3), which arises because the four input channels involved in $\langle \tilde{T}^2 \rangle$ interact with different weights due to spatial variation of the input beam.

To test the validity of the analytic prediction (3), we studied numerically the transmission matrix of a two-dimensional disordered slab embedded in a multimode waveguide, using the recursive Green’s function method [20]. The waveguide has been chosen to be wide enough that the diffusion halo at the output never reaches its walls. We compare in Fig. 3 the numerical result (2) with the analytic expression (3), for 4 different slab thicknesses and 5 different illumination areas, finding excellent agreement. Each point corresponds to an average over 100 configurations of the slab. We find that m_1 is essentially controlled by the ratio D/L , with small corrections due to $\bar{T} = \ell/L$, that appear, in particular, through the dependence of $F(\mathbf{q})$ on the “extrapolation lengths” of the disordered slab [16]. These corrections vanish in the limit $\bar{T} \rightarrow 0$. Furthermore, in the limit of a broad uniform illumination $D \gg L$, only the term $F(\mathbf{q} = \mathbf{0}) = 2/3$ contributes, and one recovers $m_1 = 1$.

Once the value of m_1 is known, the full distribution of $\tilde{t}^\dagger \tilde{t}$ follows from the FRM equations [13], which allows us to calculate the key quantity of interest for the experiments, the maximal transmission enhancement possible for a given m_1 . It is given by the upper edge of the support of the eigenvalue density on the interval $[0, 1]$. This quantity was calculated explicitly for our case,

$$\langle T^{\max} \rangle = f^{\max}(m_1, m_2 = 1, \bar{T}), \quad (4)$$

where the expression for f^{\max} is given in [13].

The analytic results given by Eqs. (4) and (3) are confirmed by simulations in a 2D-slab with excellent agreement [see Fig. 3 and the dashed line in Fig. 4 (a)]. However, it was not

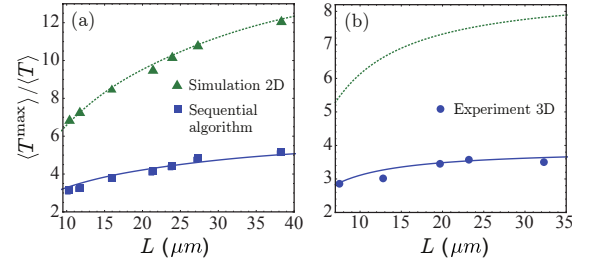


FIG. 4: (color online) Maximal transmission in a slab of thickness L , illuminated with a spot of diameter $D = 16\lambda$. (a) 2D simulations (dots), calculated with the same parameters as in Fig. (3), are compared with the theoretical prediction (solid and dashed lines) based on Eqs. (4) and (3). Due to the finite number of modes, $\langle T^{\max} \rangle$ does not exactly coincide with the upper edge of the distribution of the transmission values, which is taken into account by replacing f^{\max} by $0.91 f^{\max}$ in Eq. (4). The effect of the sequential algorithm (blue squares) is also included in the theory through the substitution $m_1 \rightarrow \alpha m_1$, with $\alpha \simeq 0.26$. (b) The 3D experiment (dots) is well described by Eq. (4), where $m_1 \rightarrow \alpha m_1$, with m_1 given by Eq. (3) solved in 3D and α identical to the 2D case.

possible to simulate numerically the transmission of a 3D-slab in the parameter regime relevant to the experiment. Moreover, experimentally we use a single photodetector, placed right behind the sample, to measure the total transmission, thus we cannot measure directly the TM \tilde{t} to access the highest transmission channels; instead we approach the maximum transmission input state using phase-only modulation and the sequential algorithm. Although it is efficient for focusing light into or through the random media, this method typically fails to find the global maximum of total transmission. We conjecture that this approach effectively reduces the control of the input channels below the value of m_1 predicted by theory by some factor, α . To estimate this factor, we run numerically a phase-only sequential algorithm on the *simulated* TM in a 2D-slab, to determine the maximum total transmission achieved with this method as a function of L , and then fit the result to the theory to get $\alpha \simeq 0.26$, which describes the 2D data well [see solid line in Fig. 4(a)]. For the experimental data from a 3D random media shown in Fig. 4(b), we find that the transmission enhancement is well below the maximum value (4), as expected due to the limitations of the optimization procedure we use. However, if we assume that the effect of this procedure is similar to its effect in 2D and make the substitution $m_1 \rightarrow 0.26 m_1$, we find good agreement. This suggests that the maximal enhancement of total transmission achieved for the samples in our experiment is limited mainly by the optimization procedure, instead of other effects such as noise in the measurements or instability of the setup.

We thank Yaron Bromberg, Brandon Redding, Sylvain Gigan and Allard Mosk for useful discussions. This study was supported in part by the facilities and staff of the Yale University Faculty of Arts and Sciences High Performance Computing Center. This work is funded by the NSF Grants ECCS-1068642.

* hui.cao@yale.edu

- [1] O. N. Dorokhov, *Solid State Communications* **51**, 381 (1984).
- [2] P. A. Mello, P. Pereyra, and N. Kumar, *Annals of Physics* **181**, 290 (1988), ISSN 0003-4916.
- [3] Y. Nazarov, *Physical Review Letters* **73**, 134 (1994), ISSN 0031-9007.
- [4] E. Akkermans, and G. Montambaux, *Mesoscopic physics of electrons and photons* (Cambridge University Press, 2007).
- [5] I. Freund, *Physica A: Statistical Mechanics and its Applications* **168**, 49 (1990).
- [6] Y. Guan, O. Katz, E. Small, J. Zhou, and Y. Silberberg, *Opt. Lett.* **37** (2012).
- [7] J. Park, C. Park, H. Yu, Y. Cho, and Y. Park, *Opt. Express* **20** (2012).
- [8] J. Park, C. Park, H. Yu, Y. Cho, and Y. Park, *Opt. Lett.* **37** (2012).
- [9] E. Small, O. Katz, Y. Guan, and Y. Silberberg, *Opt. Express* **37** (2012).
- [10] I. M. Vellekoop and A. P. Mosk, *Phys. Rev. Lett.* **101**, 120601 (2008).
- [11] M. Kim, Y. Choi, C. Yoon, W. Choi, J. Kim, Q.-H. Park, and W. Choi, *Nat. Photon.* **6**, 583 (2012).
- [12] V. A. Marčenko and L. A. Pastur, *Mathematics of the USSR-Sbornik* **1**, 457 (1967).
- [13] A. Goetschy and A. D. Stone, arXiv:cond-mat:1304.5562 (2013).
- [14] A. Aubry and A. Derode, *Phys. Rev. Lett.* **102**, 084301 (2009).
- [15] S. M. Popoff, G. Lerosey, R. Carminati, M. Fink, A. C. Boccarda, and S. Gigan, *Phys. Rev. Lett.* **104**, 100601 (2010).
- [16] Supplementary information.
- [17] I. M. Vellekoop and A. P. Mosk, *Opt. Lett.* **32**, 2309 (2007).
- [18] S. M. Popoff, A. Aubry, G. Lerosey, M. Fink, A. C. Boccarda, and S. Gigan, *Phys. Rev. Lett.* **107**, 263901 (2011).
- [19] M. C. W. van Rossum and T. M. Nieuwenhuizen, *Rev. Mod. Phys.* **71**, 313 (1999).
- [20] H. U. Baranger, D. P. DiVincenzo, R. A. Jalabert, and A. D. Stone, *Phys. Rev. B* **44**, 10637 (1991).
- [21] C. W. J. Beenakker, *Rev. Mod. Phys.* **69**, 731 (1997).
- [22] the definition of ℓ differs from the transport mean free path by a numerical coefficient [21]

Supplementary Material

Coherent control of total transmission of light through disordered media

S. M. Popoff, A. Goetschy, S. F. Liew, A. D. Stone, and H. Cao*
Department of Applied Physics, Yale University, New Haven, CT 06511, USA
(Dated: March 4, 2019)

EXPERIMENTAL SETUP

The laser beam from a Nd:YAG laser (Coherent, Compass 215M-50 SL, $\lambda = 532nm$) is expanded and projected onto a phase-only SLM (Hamamatsu, X10468-01). To control independently the two polarizations, a polarizing beam splitter attached to a right angle prism separates the two polarizations that are modulated by different areas of the SLM. A half wave-plate ensures that the incident polarization on the SLM matches its working condition. Using a 4-f system (lenses L_1 and L_2) and a beam splitter cube (BS_1) the surface of the SLM is imaged onto the entrance pupil of a microscope objective of numerical aperture 0.95. The array of the SLM can be divided into different numbers N_{in} of elements corresponding to different “macro-pixels” sizes. The diameter of the illumination area on the sample is inversely proportional to the size of the macro-pixels. The optical field is controlled with a spatial resolution of $0.95\lambda/2 \approx 280nm$. After reflection, the two polarizations are recombined on a single beam. The modulated wavefront is projected onto the pupil of a microscope objective of numerical aperture 0.95. An iris is placed at the Fourier plane of the lens L_1 to filter high spatial frequencies and allow to compensate for the 95% fill factor of the SLM. It also permits to *switch off* any segment of the SLM by displaying a high spatial frequency phase pattern. The sample is positioned at the focal plane of the microscope objective and directly on a photodetector. This way, we can measure the total transmission with an effective numerical aperture close to the unity. The maximum number of SLM segments used is $N_{in} = 1740$ which correspond to an illumination diameter of $8.3 \mu m$. To ensure the convergence of the algorithm, all segments are optimized three times in the optimization process. For $N_{in} = 1740$, the optimization takes approximately 5 hours. The laser beam from a Nd:YAG laser (Coherent, Compass 215M-50 SL, $\lambda = 532nm$) is expanded and projected onto a phase-only SLM (Hamamatsu, X10468-01). To control independently the two polarizations, a polarizing beam splitter attached to a right angle prism separates the two polarizations that are modulated by different areas of the SLM. A half wave-plate ensures that the incident polarization on the SLM matches its working condition. Using a 4-f system (lenses L_1 and L_2) and a beam splitter cube (BS_1) the surface of the SLM is imaged onto the entrance pupil of a microscope objective of numerical aperture 0.95. The array of the SLM can be divided into different numbers N_{in} of elements corresponding to different “macro-pixels” sizes. The diameter of the illumination area on the sample is inversely proportional to the size of the macro-pixels. The optical field is controlled with a spatial resolution of $0.95\lambda/2 \approx 280nm$. After reflection, the two polarizations are recombined on a single beam. The modulated wavefront is projected onto the pupil of a microscope objective of numerical aperture 0.95. An iris is placed at the Fourier plane of the lens L_1 . Filtering high spatial frequencies allows to compensate for the 95% fill factor of the SLM. It also permits to *switch off* any segment of the SLM by displaying a high spatial frequency phase pattern. The sample is positioned at the focal plane of the microscope objective and directly

into different numbers N_{in} of elements corresponding to different “macro-pixels” sizes. The diameter of the illumination area on the sample is inversely proportional to the size of the macro-pixels. The optical field is controlled with a spatial resolution of $0.95\lambda/2 \approx 280nm$. After reflection, the two polarizations are recombined on a single beam. The modulated wavefront is projected onto the pupil of a microscope objective of numerical aperture 0.95. An iris is placed at the Fourier plane of the lens L_1 to filter high spatial frequencies and allow to compensate for the 95% fill factor of the SLM. It also permits to *switch off* any segment of the SLM by displaying a high spatial frequency phase pattern. The sample is positioned at the focal plane of the microscope objective and directly on a photodetector. This way, we can measure the total transmission with an effective numerical aperture close to the unity. The maximum number of SLM segments used is $N_{in} = 1740$ which correspond to an illumination diameter of $8.3 \mu m$. To ensure the convergence of the algorithm, all segments are optimized three times in the optimization process. For $N_{in} = 1740$, the optimization takes approximately 5 hours. The laser beam from a Nd:YAG laser (Coherent, Compass 215M-50 SL, $\lambda = 532nm$) is expanded and projected onto a phase-only SLM (Hamamatsu, X10468-01). To control independently the two polarizations, a polarizing beam splitter attached to a right angle prism separates the two polarizations that are modulated by different areas of the SLM. A half wave-plate ensures that the incident polarization on the SLM matches its working condition. Using a 4-f system (lenses L_1 and L_2) and a beam splitter cube (BS_1) the surface of the SLM is imaged onto the entrance pupil of a microscope objective of numerical aperture 0.95. The array of the SLM can be divided into different numbers N_{in} of elements corresponding to different “macro-pixels” sizes. The diameter of the illumination area on the sample is inversely proportional to the size of the macro-pixels. The optical field is controlled with a spatial resolution of $0.95\lambda/2 \approx 280nm$. After reflection, the two polarizations are recombined on a single beam. The modulated wavefront is projected onto the pupil of a microscope objective of numerical aperture 0.95. An iris is placed at the Fourier plane of the lens L_1 . Filtering high spatial frequencies allows to compensate for the 95% fill factor of the SLM. It also permits to *switch off* any segment of the SLM by displaying a high spatial frequency phase pattern. The sample is positioned at the focal plane of the microscope objective and directly

on a photodiode. This way, we can estimate the total transmission with an effective numerical aperture close to the unity. The maximum number of SLM segments used is $N_{in} = 1740$ which correspond to an illumination diameter of $8.3\mu\text{m}$. To ensure the convergence of the algorithm, all segments are optimized three times in the optimization process. For $N_{in} = 1740$, the optimization takes approximately 5 hours.

The scattering samples are obtained by evaporation of a suspension of TiO_2 in a solution of water and ethanol. The suspension is poured onto a glass slide in a plastic tube. The thickness of the sample is tuned by changing the amount of solution. The mean free path ℓ estimated by the measurement of the coherent backscattering cone of a thick sample ($\geq 150\mu\text{m}$) equals $0.8 \pm 0.1\mu\text{m}$ at 532 nm. We estimate the thickness of the samples by measuring the average total transmission [1].

The cube and the prism are mounted in the same metallic holder. This is an essential part of the setup since it removes independent reflective elements in the two arms of the interferometer that may bring phase fluctuations. In light focusing experiments [2, 3], increasing the intensity on one output speckle grain only involve one column of the TM. The optimal phase of each segment of the SLM to increase the intensity at the target can be tested independently to obtain the final phase mask [4]. As a consequence, even in presence of phase fluctuations between the two polarizations, using two polarizations will generate a higher intensity enhancement at the focal spot. The enhancement of the total transmitted intensity involves the whole TM. Finding the optimal phase mask for each polarization separately and then displaying the two masks at the same time will not increase the transmission efficiency. For this reason, we expect the system to be very sensitive to phase fluctuations between two sets of controlled input channels.

As a control experiment, we test a conventional apparatus based on Mach-Zehnder interferometer [see Fig. S1(a)]. In such a configuration, light going through each arm is reflected by two separate elements. The apparatus used in the experiments presented in this paper is shown in Fig. S1(b). Since the polarizing beam splitter and the right angle prism are tightly mounted in the same holder, any vibration has the same effect on the phase of the two beams. To compare the stability of these two setups, an $\sim 100\mu\text{m}$ thick sample of average transmission $\sim 1\%$ is placed at the focal plane of the microscope objective. We first run the sequential algorithm with $N_{in} \approx 100$ segments for each polarization independently. We obtain enhancement of 1.40 and 1.44 respectively. We then run the same algorithm with both polarizations ($N_{in} \approx 2 \times 100$) for the two setups. The Mach-Zehnder configuration reaches an enhancement of 1.42, *i.e.* similar to the results for only one polarization, whereas an enhancement of 1.64 is obtained with the second setup. This proves that the interferometric stability

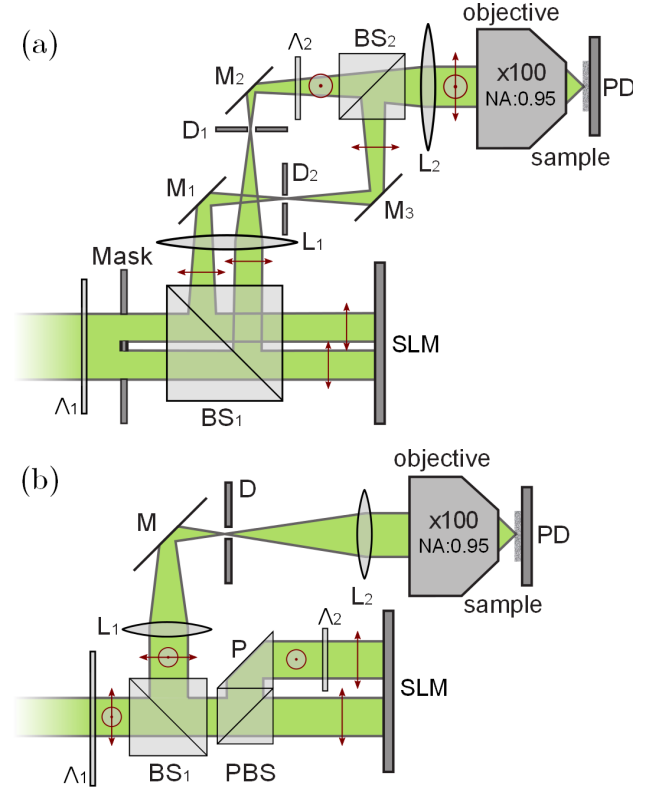


Figure S1: Two setups tested for the phase modulation of the two polarizations; (a) Mach-Zehnder configuration, (b) setup with no independent reflective elements. Λ : half-waveplate, L: lens, M: mirror, BS: beam splitter, PBS: polarizing beam splitter. The sample at the focal plane of the microscope objective (100x, NA = 0.95) is a scattering layer of TiO_2 particles. For the sake of clarity, the two photodetectors and the beam splitter used to measure the input and reflected intensity are not shown.

of the setup presented in this paper is good enough to take advantage of the modulation of the two polarizations. We tested the two setups with different samples and for different numbers of pixels and obtained similar results to the above. As a control experiment, we test a conventional apparatus based on Mach-Zehnder interferometer [see Fig. S1(a)]. In such a configuration, light going through each arm is reflected by two separate elements. The apparatus used in the experiments presented in this paper is shown in Fig. S1(b). Since the polarizing beam splitter and the right angle prism are tightly mounted in the same holder, any vibration has the same effect on the phase of the two beams. To test the stability of these two setups, a $\approx 100\mu\text{m}$ thick sample of average transmission $\approx 1\%$ is placed at the focal plane of the microscope objective. We first run the sequential algorithm with $N_{in} \approx 100$ segments for each polarization independently. We obtain enhancement of 1.40 and 1.44 respectively. We then run the same algorithm with both polarizations ($N_{in} \approx 2 \times 100$) for the two setups. The

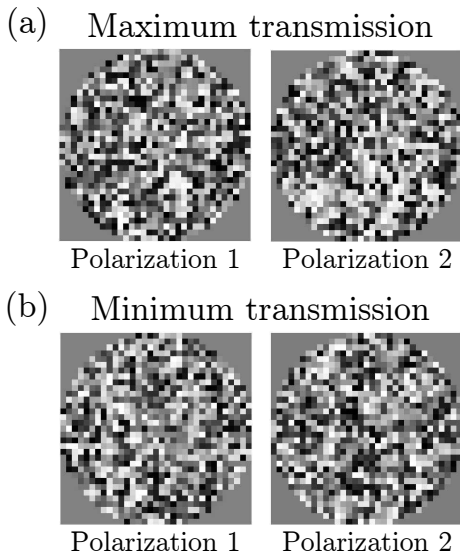


Figure S2: Optimized phase masks for the two polarizations that correspond to the enhancement (a) and the reduction (b) of the total transmission.

Mach-Zehnder configuration reaches an enhancement of 1.42, *i.e.* similar to the results for only one polarization, whereas an enhancement of 1.64 is obtained with the second setup. This proves that the interferometric stability of the setup presented in this paper is good enough to take advantage of the modulation of the two polarizations. We tested the two setups with different samples and for different numbers of pixels with similar results.

OPTIMAL PHASE MASKS

Various artifacts can cause misleading results when trying to optimize the total transmission by measuring solely the intensity transmitted through the scattering medium. On one hand, compensating for the optical aberrations or misalignment of the optical system between the SLM and the sample would increase the throughput. On the other hand, generating a phase mask that deflects part of the input light away from the scattering sample would decrease the measured transmitted intensity. Such cases would correspond to regular patterns of the SLM with low spatial frequencies. We show in Fig. S2 the phase masks for both polarizations corresponding to the maximal increase and maximal decrease of the total transmission presented in Fig. 2 of the main text. The pseudo-random appearance of these phase masks indicates the absence of obvious artifact in the optimization when measuring the ratio of the transmitted intensity to the input intensity.

TRANSMISSION EIGENVALUE DENSITY AND FILTERED RANDOM MATRIX ENSEMBLE

In this section, we describe how we generated numerically the transmission eigenvalue density for a slab illuminated with a finite illumination area, and show that this density is well described by the filtered random matrix (FRM) ensemble.

The transmission matrix is defined as the transmission operator \hat{t} expressed in a unit-flux basis, $\{\psi_a\}$; the matrix elements of the TM are $t_{ba} = \langle \psi_b | \hat{t} | \psi_a \rangle$. If we use the set of transverse plane waves $\chi_a(\rho)$ normalized by their flux, $\psi_a(\rho) = \langle \rho | \psi_a \rangle$ is given by

$$\psi_a(\rho) = \frac{1}{\sqrt{\mu_a}} \chi_a(\rho) = \frac{1}{\sqrt{A\mu_a}} e^{i\mathbf{q}_a \cdot \rho}, \quad (\text{S1})$$

where A is the area of the slab, ρ is the transverse coordinate, and $\mu_a = \sqrt{1 - q_a^2/k^2} = \cos(\theta_a)$, with θ_a the angle of the channel a with respect to the longitudinal axis of the slab. To model the effect of the focused spot illumination, we introduce a projector in real space,

$$\hat{P} = \int d\rho s(\rho) |\rho\rangle \langle \rho|, \quad (\text{S2})$$

where $s(\rho)$ is the transverse profile of the illumination field. In this situation, the elements of the accessible transmission matrix, \tilde{t} , are

$$\tilde{t}_{ba} = \langle \psi_b | \hat{t} \hat{P} | \psi_a \rangle. \quad (\text{S3})$$

In matrix form, \tilde{t} can be expressed as

$$\tilde{t} = t \tilde{P}, \quad (\text{S4})$$

$$\tilde{P} = \mu^{1/2} \chi P \chi^\dagger \mu^{-1/2}, \quad (\text{S5})$$

where μ is a diagonal matrix with matrix elements $\{\mu_a\}$, χ is a unitary matrix representing a change of basis from $\{\chi_a\}$ to $\{\rho\}$ (in this case just the inverse Fourier transform), and P is the matrix representation of the operator (S2).

As explained in the main text, we used the recursive Green's function method to build the transmission matrix of the disordered slab, t , from the solution of the Helmholtz equation, $[\nabla^2 + k^2 \epsilon(\mathbf{r})] \psi(\mathbf{r}) = 0$ [5]. The slab is embedded in a multimode waveguide supporting a number N of transverse propagating channels, its width is large enough so that the diffusion halo at the output never reaches the boundaries of the guide. We chose a uniform illumination profile $s(\rho)$, that covers a segment of length D in two-dimensions or a disk of diameter D in three dimensions, constructed the matrix \tilde{t} according to Eqs. (S4) and (S5), and found numerically the non-zero eigenvalues of $\tilde{t}^\dagger \tilde{t}$ for different realizations of the dielectric function $\epsilon(\mathbf{r}) = n_0^2 + \delta\epsilon(\mathbf{r})$, where $\delta\epsilon(\mathbf{r})$ is uniformly distributed between $[-\epsilon_{sc}, \epsilon_{sc}]$ inside the slab and $\delta\epsilon(\mathbf{r}) = 0$

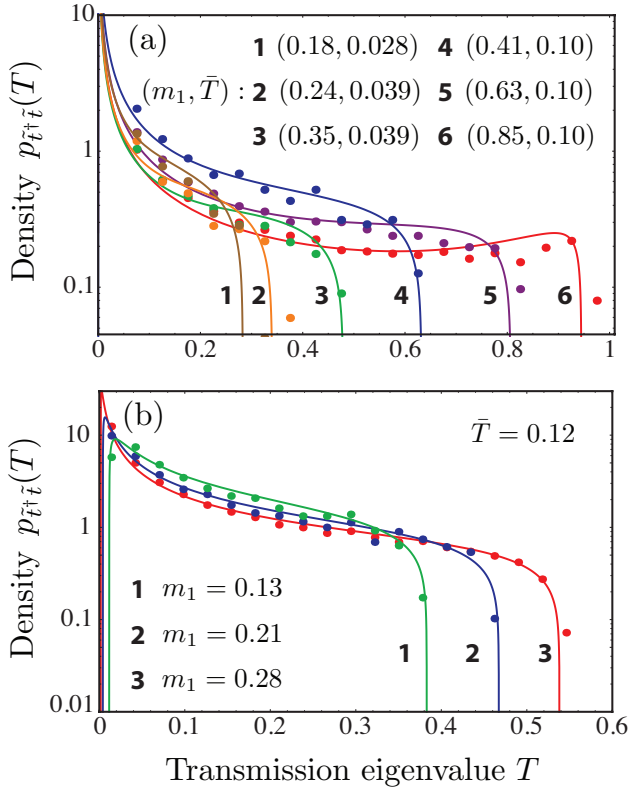


Figure S3: Transmission eigenvalue density of a disordered slab illuminated by a focused spot in 2D (a) and 3D (b), for different values of the slab thickness L and the illumination diameter D . Numerical results (dots) are compared with the FRM prediction (S6) (solid lines), where $\bar{T} = \langle \text{Tr}(t^\dagger t) \rangle / N$ is found from the simulation with complete illumination ($s(\rho) = 1$ on the full surface corresponds to $m_1 = 1$) and $m_1 = \text{Var} \tilde{T} / (2\bar{T}/3 - \bar{T}^2)$, with $\text{Var} \tilde{T}$ the variance of the numerical distribution. We generated 100 realizations of the slab in 2D and 30 realizations in 3D, with a dielectric function parametrized by $n_0 = 1.3$ and $\epsilon_{sc} = 1.02$ in 2D, $n_0 = 1.4$ and $\epsilon_{sc} = 1.39$ in 3D (see text for details). Values of (kD, kL, N) : (a) (63, 450, 473), (64, 320, 405), (104, 320, 405), (60, 120, 270), (129, 120, 270), (336, 120, 270), (b) (15, 30, 1419), (22.5, 30, 1419), (30, 30, 1419).

outside. The value of ϵ_{sc} is tuned to have different values of the mean free path.

We now compare the density of the non-zero eigenvalues of $\tilde{t}^\dagger \tilde{t}$ with the prediction of the FRM ensemble. The latter is characterized by an eigenvalue density, $p_{\tilde{t}^\dagger \tilde{t}}(T)$, parametrized by a fraction m_1 (m_2) of the input (output) channels controlled (measured), and by the average transmission with complete channel control, $\bar{T} = \langle \text{Tr}(t^\dagger t) \rangle / N$. When all output channels are collected, and a *randomly chosen* subset of input channels are controlled, then $m_2 = 1$, and m_1 is equal to the ratio of the variance of the non-zero eigenvalues of $\tilde{t}^\dagger \tilde{t}$, $\text{Var} \tilde{T}$, to the variance of the eigenvalues of $t^\dagger t$, $\text{Var} T = 2\bar{T}/3 - \bar{T}^2$. This is an exact relation within the FRM. Since here we are interested in focused spot illumi-

nation, i.e. correlated input channels, we conjecture that this relationship still holds to a good approximation, and use it to calculate m_1 . According to Ref. [6], the FRM distribution of interest is given by

$$p_{\tilde{t}^\dagger \tilde{t}}(T) = -\frac{1}{\pi} \lim_{\eta \rightarrow 0^+} \text{Im} g_{\tilde{t}^\dagger \tilde{t}}(T + i\eta), \quad (\text{S6})$$

where $g_{\tilde{t}^\dagger \tilde{t}}(z)$ is the solution of

$$g_{\tilde{t}^\dagger \tilde{t}}(z) = \frac{1}{m_1} g_{t^\dagger t} \left(z + \frac{1 - m_1}{m_1 g_{\tilde{t}^\dagger \tilde{t}}(z)} \right), \quad (\text{S7})$$

$g_{t^\dagger t}(z)$ is the resolvent of the matrix $t^\dagger t$,

$$g_{t^\dagger t}(z) = \frac{1}{z} - \frac{\bar{T}}{z\sqrt{1-z}} \text{Arctanh} \left[\frac{\text{Tanh}(1/\bar{T})}{\sqrt{1-z}} \right], \quad (\text{S8})$$

and $m_1 = \text{Var} \tilde{T} / \text{Var} T$. We compared the theoretical prediction (S6) to the result of numerical simulations, in both two and three dimensions, for different values of D , L , n_0 , ϵ_{sc} , and always found a good agreement. Some representative results are shown in Fig. S4(a) (2D simulations) and Fig. S4(b) (3D simulations). They confirm that the predictions of the FRM ensemble hold in the open slab geometry illuminated by a focused spot.

PROOF OF EQ. (3) OF THE MAIN TEXT

To compute the variance $\text{Var} \tilde{T}$ introduced in Eq. (2) of the main text, we need to evaluate

$$\langle \tilde{T}^2 \rangle = \frac{1}{N} \langle \text{Tr}(\tilde{t}^\dagger \tilde{t} \tilde{t}^\dagger \tilde{t}) \rangle, \quad (\text{S9})$$

where N is the number of transverse channels; later we shall take $N \rightarrow \infty$. With the help of the representation (S4), Eq. (S9) becomes

$$\langle \tilde{T}^2 \rangle = \sum_{\substack{a_1, a_2, a_3, a_4 \\ b, b'}} \frac{(\tilde{P}\tilde{P}^\dagger)_{a_1 a_4} (\tilde{P}\tilde{P}^\dagger)_{a_3 a_2}}{N} \langle t_{ba_1} t_{ba_2}^* t_{b'a_3} t_{b'a_4}^* \rangle. \quad (\text{S10})$$

At this stage, it is convenient to express the transmission amplitudes t_{ba} in terms of the elements $G_{ba} = \langle \chi_b, z = L | \hat{G} | \chi_a, z = 0 \rangle$ of the retarded Green's function of the scalar Helmholtz equation, $\hat{G} = \lim_{\eta \rightarrow 0^+} [\nabla^2 + k^2 \epsilon(\mathbf{r}) + i\eta]^{-1}$; it is given by $t_{ba} = 2ik\sqrt{\mu_b \mu_a} G_{ba}$ [7]. In this way, Eq. (S10) involves the average of the product of four Green's functions that can be evaluated by means of diagrammatic methods developed for wave transport. In the limit $\bar{T} \ll 1$, the leading term in the diagrammatic expansion of (S10) is a connected loopless diagram corresponding to two incoming diffusons interacting inside the sample through a Hikami vertex, where they exchange amplitudes. Such a diagram is typically responsible for long-range correlations of the speckle pattern.

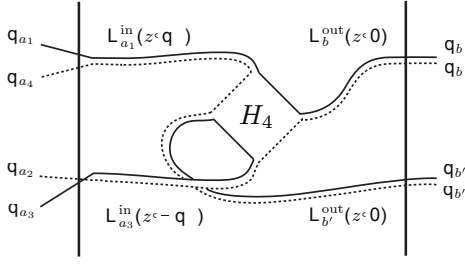


Figure S4: Connected loopless diagram contributing to the second moment (S10). It involves one diffusion crossing through a Hikami four-point vertex H_4 .

Since Eq. (S10) contains a sum over the output channels b and b' , only outgoing diffusons with no transverse momentum contribute significantly to $\langle \tilde{T}^2 \rangle$. This implies that diagrams with equal b_i are paired into diffusons. On the other hand, since a Hikami vertex conserves momentum, the two incoming diffusons must have opposite transverse momentum \mathbf{q}_α : $\mathbf{q}_{a_1} - \mathbf{q}_{a_4} = \mathbf{q}_{a_2} - \mathbf{q}_{a_3} = \mathbf{q}_\alpha$ (see Fig. S4). After summation over the output channels, Eq. (S10) reduces to

$$\langle \tilde{T}^2 \rangle = \sum_{a_1, a_3, \alpha} \frac{(\tilde{P}\tilde{P}^\dagger)_{a_1(a_1-\alpha)}(\tilde{P}\tilde{P}^\dagger)_{a_3(\alpha-a_3)}}{N} K_{a_1 a_3}(\mathbf{q}_\alpha), \quad (\text{S11})$$

where the kernel $K_{a_1 a_3}(\mathbf{q})$ has the generic form

$$K_{a_1 a_3}(\mathbf{q}_\alpha) = 2h_4 A \int_0^L dz \mathcal{L}_{a_1}^{\text{in}}(z, \mathbf{q}_\alpha) \mathcal{L}_{a_3}^{\text{in}}(z, -\mathbf{q}_\alpha) \times [\partial_z \mathcal{L}^{\text{out}}(z, \mathbf{0})]^2. \quad (\text{S12})$$

Here $\mathcal{L}_a^{\text{in}}(z, \mathbf{q})$ is the diffuse intensity with transverse momentum \mathbf{q} , evaluated at a distance z from the sample surface, and created from a beam impinging in direction a ; similarly, $\mathcal{L}^{\text{out}} = \sum_b \mathcal{L}_b^{\text{out}}$ is the outgoing diffuse intensity (see Ref. [8] for the explicit expression of $\mathcal{L}_a^{\text{in/out}}$ in 3D). The prefactor h_4 is the weight of the Hikami four-point vertex [8, 9]. Note that to obtain Eq. (S12) we assumed the slab to be wide enough in order to have translational invariance along the transverse direction(s).

We proceed further by assuming that the matrices $\mu^{1/2}$ and $\mu^{-1/2}$ that appear in the definition (S5) of \tilde{P} do not affect significantly the eigenvalue distribution of $\tilde{t}^\dagger \tilde{t}$. We checked numerically the validity of this assumption. This allows us to simplify the matrix elements $(\tilde{P}\tilde{P}^\dagger)_{aa'}$ as

$$(\tilde{P}\tilde{P}^\dagger)_{aa'} \simeq \int d\rho s(\rho)^2 \chi_a^*(\rho) \chi_{a'}(\rho) = \frac{I(\mathbf{q}_{a'} - \mathbf{q}_a)}{A}, \quad (\text{S13})$$

where $I(\mathbf{q})$ is the Fourier transform of the transverse input intensity profile $s(\rho)^2$. The second moment (S11) becomes

$$\langle \tilde{T}^2 \rangle = \sum_{\mathbf{q}} \frac{I(\mathbf{q})I(-\mathbf{q})}{NA^2} K(\mathbf{q}), \quad (\text{S14})$$

with $K(\mathbf{q}) = \sum_{a_1 a_3} K_{a_1 a_3}(\mathbf{q})$. Using Eq. (S12), we find that $K(\mathbf{q})$ is proportional to the long range-correlations of the speckle pattern $C_2(\mathbf{q}) = \langle T_a T_{a'} \rangle / \langle T_a \rangle \langle T_{a'} \rangle - 1$,

$$K(\mathbf{q}) = g^2 C_2(\mathbf{q}) = gF(\mathbf{q}), \quad (\text{S15})$$

where $T_a = \sum_b |t_{ba}|^2$ is the total transmission of the incoming channel a , \mathbf{q} is the perpendicular momentum difference of the channels a and a' , $g = \langle \text{Tr}(t^\dagger t) \rangle = NT$ is the optical dimensionless conductance, and $F(\mathbf{q})$ is given by

$$F(\mathbf{q}) \equiv g C_2(\mathbf{q}) = \frac{\sinh(2qL) - 2qL + f_1(qz_0, qL)}{2qL \sinh(qL)^2 + f_2(qz_0, qL)}. \quad (\text{S16})$$

In this expression, z_0 is the extrapolation length of the slab and the two functions $f_1(qz_0, qL)$ and $f_2(qz_0, qL)$ are polynomials in qz_0 that vanish in the limit $z_0 \ll L$. The explicit form of the latter can be found in Ref. [8]. Note that, although the expressions of both $\mathcal{L}^{\text{in/out}}$ and h_4 in Eq. (S12) depend on the transverse space dimension, the result (S16) does not, except through the explicit expression of z_0 in terms of the mean free path. In the continuous limit $N \rightarrow \infty$, Eqs. (S14) and (S15) yield

$$\langle \tilde{T}^2 \rangle = \frac{\bar{T}}{A} \int d\mathbf{q} \frac{I(\mathbf{q})I(-\mathbf{q})}{(2\pi)^{d-1}} F(\mathbf{q}), \quad (\text{S17})$$

where d is the space dimension.

Similarly, we can express the first moment $\langle \tilde{T} \rangle = \langle \text{Tr}(t^\dagger t) \rangle / N$ as

$$\langle \tilde{T} \rangle = \frac{1}{N} \sum_{a, a', b} (\tilde{P}\tilde{P}^\dagger)_{aa'} \langle t_{ba} t_{ba'}^* \rangle. \quad (\text{S18})$$

Since the outgoing diffusons have no transverse momentum, the leading term in this expression is the loopless diagram corresponding to $a = a'$, so that $\langle \tilde{T} \rangle = \sum_a (\tilde{P}\tilde{P}^\dagger)_{aa} \langle T_a \rangle / N$. Neglecting once again the effect of the matrix μ in the definition of \tilde{P} , we obtain with Eq. (S13)

$$\langle \tilde{T} \rangle = \frac{I(\mathbf{q} = \mathbf{0})}{A} \bar{T}. \quad (\text{S19})$$

This allows us to express the second moment (S17) as

$$\langle \tilde{T}^2 \rangle = \langle \tilde{T} \rangle \int d\mathbf{q} \frac{I(\mathbf{q})I(-\mathbf{q})}{(2\pi)^{d-1} I(\mathbf{q} = \mathbf{0})} F(\mathbf{q}). \quad (\text{S20})$$

In the case of a uniform illumination over an area $A_0 < A$, the matrix \tilde{t} is of size $N \times N$ but of rank $A_0 N / A$. Hence, a fraction $(1 - A_0/A)$ of its eigenvalues are equal to zero. In the present study, we are interested in the density of non-zero eigenvalues,

$$p_{T \neq 0}(T) = \frac{A}{A_0} p(T) - \left(\frac{A}{A_0} - 1 \right) \delta(T), \quad (\text{S21})$$

whose moments are $\langle \tilde{T}^n \rangle_{T \neq 0} = (A/A_0) \langle \tilde{T}^n \rangle$, for all $n \in \mathbb{N}$. Thus the relation (S20) holds for non-zero eigenvalues, with $\langle \tilde{T} \rangle_{T \neq 0} = \bar{T}$. Using $\text{Var}T = 2\bar{T}/3 - \bar{T}^2$, we finally obtain

$$\begin{aligned}
 m_1 &\equiv \frac{\langle \tilde{T}^2 \rangle_{T \neq 0} - \langle \tilde{T} \rangle_{T \neq 0}^2}{\text{Var}T} \\
 &= \frac{1}{2/3 - \bar{T}} \left[\int d\mathbf{q} \frac{I(\mathbf{q})I(-\mathbf{q})}{(2\pi)^{d-1}I(\mathbf{q}=\mathbf{0})} F(\mathbf{q}) - \bar{T} \right], \tag{S22}
 \end{aligned}$$

which is Eq. (3) of the main text.

* hui.cao@yale.edu

- [1] J. G. Rivas, R. Sprik, C. M. Soukoulis, K. Busch, and A. Lagendijk, *Europhysics Letters (EPL)* **48**, 22 (1999), ISSN 0295-5075.
- [2] I. M. Vellekoop and A. P. Mosk, *Opt. Lett.* **32**, 2309 (2007).
- [3] S. M. Popoff, G. Lerosey, M. Fink, A. C. Boccara, and S. Gigan, *Nat. Commun.* **1**, 1 (2010).
- [4] I. Vellekoop and A. Mosk, *Optics Communications* **281**, 3071 (2008), ISSN 00304018, 0710.3295.
- [5] H. U. Baranger, D. P. DiVincenzo, R. A. Jalabert, and A. D. Stone, *Phys. Rev. B* **44**, 10637 (1991).
- [6] A. Goetschy and A. D. Stone (2013), arXiv:cond-mat:1304.5562.
- [7] D. S. Fisher and P. A. Lee, *Phys. Rev. B* **23**, 6851 (1981).
- [8] M. C. W. van Rossum and T. M. Nieuwenhuizen, *Rev. Mod. Phys.* **71**, 313 (1999).
- [9] E. Akkermans, *Mesoscopic physics of electrons and photons* (Cambridge University Press, 2007).